

This work was written as part of one of the author's official duties as an Employee of the United States Government and is therefore a work of the United States Government. In accordance with 17 U.S.C. 105, no copyright protection is available for such works under U.S. Law.

Public Domain Mark 1.0

<https://creativecommons.org/publicdomain/mark/1.0/>

Access to this work was provided by the University of Maryland, Baltimore County (UMBC) ScholarWorks@UMBC digital repository on the Maryland Shared Open Access (MD-SOAR) platform.

Please provide feedback

Please support the ScholarWorks@UMBC repository by emailing scholarworks-group@umbc.edu and telling us what having access to this work means to you and why it's important to you. Thank you.



Optical Characterization of the DART Impact Plume: Importance of Realistic Ejecta Scattering Properties

Ramin Lolachi^{1,2,3} , David A. Glenar^{1,2,3} , Timothy J. Stubbs² , and Ludmilla Kolokolova⁴

¹ Center for Space Sciences and Technology, University of Maryland, Baltimore County, Baltimore, MD 21250, USA; rlolachi@umbc.edu, ramin.lolachi@nasa.gov

² NASA Goddard Space Flight Center, Greenbelt, MD 20771, USA

³ Center for Research and Exploration in Space Science and Technology, NASA/GSFC, Greenbelt, MD 20771, USA

⁴ University of Maryland, College Park, MD 20742, USA

Received 2022 September 30; revised 2022 November 29; accepted 2022 December 5; published 2023 February 6

Abstract

The Double Asteroid Redirection Test (DART) mission will impact the moon Dimorphos of the (65803) Didymos binary and demonstrate the kinetic impactor technique for planetary defense. Observations from the ride-along CubeSat companion, LICIACube, of the spatial structure and temporal evolution of the resulting ejecta plume will help determine the vector momentum transfer and constrain physical properties such as strength and porosity. The optical scattering properties of the ejecta particles used in plume simulations will dictate the critical relation between observed brightness and inferred ejecta mass (and momentum). Here we examine the scattering behavior of plausible analogs for Dimorphos ejecta particles, including laboratory-measured “millimeter grains” selected based on a comparison with Bennu particle photometry. Over the range of phase angles observable by LICIACube ($\lesssim 120^\circ$), brightness simulations for optical depths ranging from 0.01 to 10 show that scattering from these analogs is considerably dimmer than from grains scattering isotropically. Therefore, adopting realistic scattering properties for ejecta particles is critical for accurately interpreting and understanding observations of the DART impact.

Unified Astronomy Thesaurus concepts: Asteroid satellites (2207); Asteroids (72); Impact phenomena (779); Near-Earth objects (1092); Radiative transfer (1335); Radiative transfer simulations (1967)

1. Introduction

As the world’s first planetary defense mission, the Double Asteroid Redirection Test (DART) spacecraft aims to demonstrate asteroid deflection by kinetic impact by colliding with the moon Dimorphos, the secondary in the (65803) Didymos binary system, and modifying its orbit through momentum transfer (Cheng et al. 2018; Rivkin et al. 2021). The DART mission was launched on 2021 November 24 and predicted to impact Dimorphos at 6.145 km s^{-1} in a direction approximately opposite to its orbital velocity (i.e., impacting the leading hemisphere causing Dimorphos to have a shorter orbital period) on 2022 September 26 (Cheng et al. 2022). Observations by ground-based telescopes will measure the change in the orbital period of Dimorphos resulting from the DART impact (target of at least 73 s; Rivkin et al. 2021). Additionally, the impact and resulting ejecta will be observed by the Light Italian CubeSat for Imaging of Asteroids (LICIACube), a ride-along CubeSat that will separate from the DART spacecraft a few days before impact (Dotto et al. 2021). The DART mission has a Level 1 requirement to measure the momentum transfer efficiency of the impact β and characterize the resulting effects of the impact (Feldhacker et al. 2017; Cheng et al. 2018, 2020, 2022; Rainey et al. 2020; Stickle et al. 2020; Rivkin et al. 2021).

The momentum transfer efficiency (or enhancement) parameter, β , is defined as

$$\beta = \frac{p_{\text{target}}}{p_{\text{impactor}}} = 1 + \frac{p_{\text{ejecta}}}{p_{\text{impactor}}}, \quad (1)$$

where p_{target} is the 3D vector momentum change for Dimorphos, p_{impactor} is the momentum of the DART spacecraft just prior to impact, and p_{ejecta} is the momentum carried by the escaping ejecta material (Rainey et al. 2020; Stickle et al. 2020; Cheng et al. 2022). As a consequence of the escaping ejecta, it is possible to have a value $\beta \geq 1$, i.e., an enhanced momentum change that is larger than the incoming spacecraft momentum, p_{impactor} (Rivkin et al. 2021).

From Equation (1), it is evident that characterizing p_{ejecta} is vital to fully understanding β . The resulting plume properties (including brightness), ejecta momentum, and, consequently, β are controlled by several global factors related to the asteroid material: strength, porosity (micro- and macroscopic), cohesiveness (do particles stick together?), and internal structure (e.g., is it a “rubble pile”? is there a regolith layer present?; Raducan et al. 2020; Stickle et al. 2020). However, factors local to the impact site can alter the value for β : surface slope relative to incident direction, local topography (Feldhacker et al. 2017), and whether DART impacts into a boulder or regolith (Stickle et al. 2017).

The complex interplay of factors causes β to be degenerate, i.e., multiple scenarios can give the same value. Earth-based measurements of the orbital period change can only determine the transverse velocity change, i.e., the velocity change component along the orbital motion (Cheng et al. 2020). Therefore, to constrain the factors controlling β , it is also important to make plume ejecta observations in situ. Optical



Original content from this work may be used under the terms of the [Creative Commons Attribution 4.0 licence](https://creativecommons.org/licenses/by/4.0/). Any further distribution of this work must maintain attribution to the author(s) and the title of the work, journal citation and DOI.

Table 1
LICIACube Camera Specification

Imager	LEIA	LUKE
IFOV ($\mu\text{rad pixel}^{-1}$)	25	78
FOV (deg)	2.9×2.9	9.2×4.9
Bandpass (nm)	Panchromatic: 400–900	RGB Bayer filter
Aperture (cm)	7.6	1.4
Focal length (cm)	22.3	7.1
Focal ratio (f/n)	3	5

observations from LICIACube of the evolving plume brightness and ejecta direction, coupled with radiative transfer modeling of the sunlight scattered by the ejecta particles, can provide critical information. Examples of this are the developing spatial and mass distribution of ejecta material, particle shape and composition, and properties of the target asteroid, such as strength and porosity (Cheng et al. 2020). Numerical impact simulations used to calculate β will use the above information as input to determine or constrain ejecta and asteroid properties (Cheng et al. 2020; see their Figure 2). Two imagers on board LICIACube will capture the impact: the LICIACube Explorer Imaging for Asteroid (LEIA) narrow-field monochrome camera and the LICIACube Unit Key Explorer (LUKE) wide-field RGB camera (Dotto et al. 2021; Cheng et al. 2022). For reference, camera specifications are given in Table 1. Resolution at closest approach ($t \approx 167$ s after impact; Figure 4) for LEIA is 1.4 m pixel^{-1} and for LUKE is 4 m pixel^{-1} .

Imaging and subsequent analysis of artificially created hypervelocity impacts on small bodies is not without precedent, for instance, the 360 kg impactor on board Deep Impact hitting comet nucleus 9P/Tempel 1 (A’Hearn et al. 2005) with radiative transfer plume brightness models/reconstruction by Nagdimunov et al. (2014) and the 2 kg Small Carry-on Impactor on board Hayabusa2 on Ryugu (Arakawa et al. 2020) with ejecta particle size determination by Wada et al. (2021).

Figure 1 shows a high-level overview of the retrieval of ejecta properties, in which the fragment scattering models developed in this study play a critical role (see orange box highlighted in black). The top line shows the input required for this method. On the right (blue boxes) are inputs known with some confidence: the LICIACube pointing geometry and the spacecraft’s camera specifications refined by instrument calibration. Input quantities on the left (orange boxes) are initially constrained only by the results of previous studies and then refined as the data analysis proceeds. One of these is the scattering model, specifically, the effective phase curve shape and single-scattering albedo.

One can then plug these into observing simulations combined with models of plume optical depth (and therefore mass evolution). This results in a simulated image sequence that can be compared against the real observations. The parameters on these models are iterated until convergence, i.e., until the simulation results match the LICIACube observations. This then allows one to calculate ejecta mass and help constrain ejecta momentum. Our study is not intended as a plume model or retrieval but instead focuses on one vital component, testing the importance of using plausible plume ejecta grain scattering properties models (orange box highlighted with black outline). Without an accurate scattering model, estimates of ejecta mass and momentum, which depend on these, remain largely

uncertain (in some cases by more than an order of magnitude). Plume ejecta will likely be dominated by large particles (larger than hundreds of microns) because of a coarse regolith and rubble-pile surface. This is supported by results from Gundlach & Blum (2013), who found that regolith grain size on airless bodies scales inversely with object size, with average grain sizes in the $10\text{--}100 \mu\text{m}$ region for large objects (e.g., the Moon) and the millimeter/centimeter regime for objects with diameters less than ~ 100 km. Given the small diameter of Dimorphos (164 m; Cheng et al. 2022), large particles are to be expected. Using Figure 11 from Gundlach & Blum (2013) and a surface gravity of $5 \times 10^{-5} \text{ m s}^{-2}$ (Ritter et al. 2021), the average grain size on Dimorphos is predicted to be $\sim 1 \times 10^4 \mu\text{m}$ (~ 1 cm).

Further evidence for this size regime of particles comes from asteroid Ryugu (diameter ≈ 900 m), where typical ejecta particle sizes were in the range of several centimeters to decimeters with an absence of millimeter-sized particles (Wada et al. 2021). Another case that provides a close analog for the DART impact is the putative impact on the active asteroid P/2010 A2 (diameter ≈ 120 m), where most observations imply particle sizes in the millimeter-to-centimeter regime (Jewitt et al. 2010; Snodgrass et al. 2010; Hainaut et al. 2012) with a corresponding power-law slope of -3.3 to -3.5 . However, there is the exception of a $10 \mu\text{m}\text{--}1$ cm range inferred by Moreno et al. (2010). An additional similarity to Dimorphos, assumed to be an S-type asteroid (de León et al. 2006), comes from the fact that P/2010 A2 is an Sq type (Kim et al. 2012). It is also likely that the impact velocity, though unknown, would have been around the average velocity for main-belt asteroids, $4\text{--}5 \text{ km s}^{-1}$ (Farinella & Davis 1992), comparable to the $\approx 6 \text{ km s}^{-1}$ for DART (Cheng et al. 2018; Rivkin et al. 2021). However, one significant difference is the inferred impactor radius of ~ 10 m (Jewitt et al. 2010), which is much larger than DART. Despite this, the expected ejecta bulk velocity of 0.2 m s^{-1} is comparable to that of DART (Fahnestock et al. 2022).

Given the evidence above, it is reasonable to assume that the scattering properties for the resulting ejecta fragments (synonymous with particles, though due to the large expected size, this terminology is deemed appropriate by the authors) will be in the geometric domain with size parameter $X = 2\pi a/\lambda \gg 1$, i.e., radius (a) \gg wavelength (λ) (Hapke 2012). Phase curves and albedos for particles in this size range depend not only on refractive index but also on shape, surface roughness, and roughness scale. Large-grain ray-tracing models that mimic surface roughness using a mantle-core geometry have achieved some success in reproducing scattering behavior observed in the lab, but the results are mixed (Muñoz et al. 2007, 2017, 2020; Muinonen et al. 2009; Nousiainen et al. 2011; Escobar-Cerezo et al. 2017). To avoid model-related uncertainties, we examine a small set of plausible phase functions obtained from lab scattering measurements of large (“millimeter-grain”) particles (Muñoz et al. 2012, 2017, 2020). This set of analogs was further down-selected using the results of Bennu particle photometry by OSIRIS-Rex (Hergenrother et al. 2020). The single-scattering albedo of these grains is estimated using the measured brightness of the Didymos–Dimorphos system, followed by an albedo correction.

Though large particles/fragments are expected, it is prudent to consider the plume brightness contribution from a possible fine-grain population in light of results by Moreno et al. (2010)

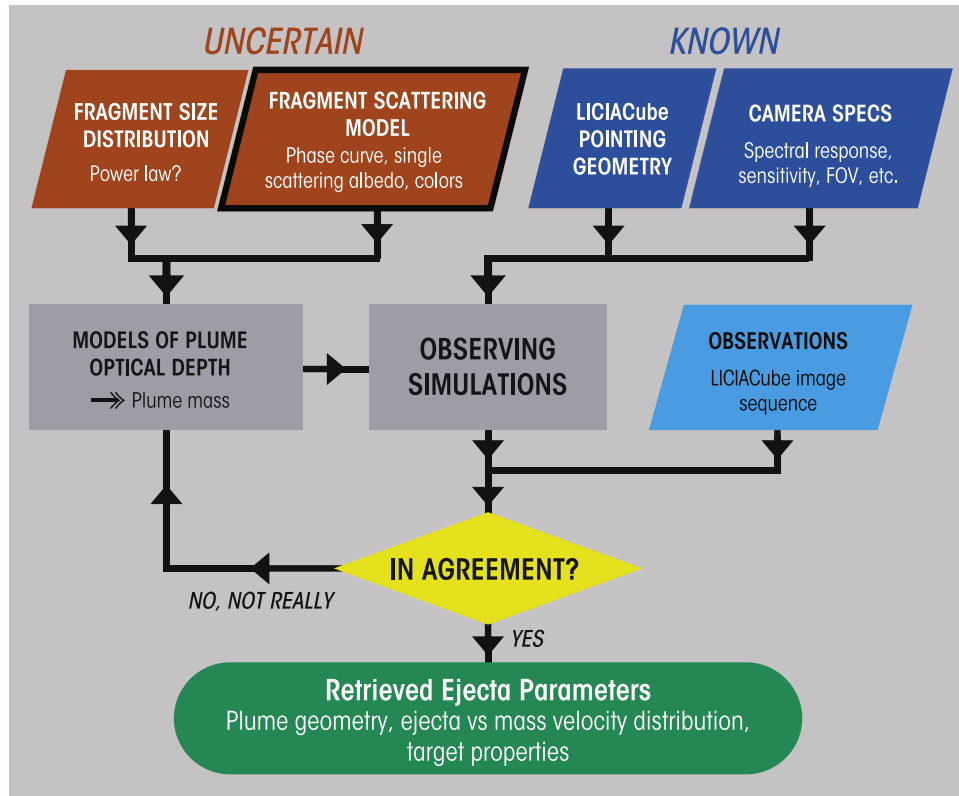


Figure 1. Flow diagram illustrating a broadly defined approach for estimating the mass of the ejecta plume material from LICIACube images, in which the fragment scattering models developed in this study play a critical role (orange box highlighted with a black outline). The top line shows “known” input parameters that are obtained from either direct pointing or instrument calibration (blue) and “uncertain” quantities (orange) that begin only as trial values constrained by previous studies but iteratively improve as data reduction evolves. Observing simulation results are compared with LICIACube observations (light blue). If they are not in agreement, then the plume model parameters are adjusted and the comparison is repeated, iterating toward convergence. The fragment scattering properties are a critical component in this methodology, without which the retrieved parameters will be inaccurate, potentially by more than an order of magnitude. Our results highlight the importance of using realistic ejecta scattering parameters and shows how this influences the modeling uncertainties.

for asteroid P/2010 A2 and the possible effects of impact processing on the particle size distribution (Cheng et al. 2016). We therefore include the phase curves of somewhat smaller grains represented by measurements of sand particles (Muñoz et al. 2007). The methodology described here, which consists of laboratory scattering measurements and supporting geometric modeling results, can also be adapted and applied to other asteroids.

In Section 2, we discuss the LICIACube viewing geometry and model setup for our plume brightness simulation. In Section 3, we discuss the method for deriving plausible phase curves for the ejecta plume fragments, as well as their scattering properties. In Section 4, these models are applied to create plume brightness simulations from the perspective of LICIACube at three representative time steps. Finally, in Section 5, we summarize the implications of our findings on the plume observations and their interpretation.

2. Modeling the Plume Impact Brightness

2.1. Scattering from an Optically Thin Layer

We used plume fragment scattering properties models to compute the visible-wavelength brightness of the DART impact plume as observed from the LICIACube flyby perspective. These scattering properties models are derived from laboratory measurements by Muñoz et al. (2007, 2017, 2020) and further constrained by photometry of naturally

occurring ejecta particles from Bennu (Hergenrother et al. 2020) as discussed in Section 3.

Following Cheng et al. (2020), we conceptualize the DART impact plume as an expanding cone with an approximate opening angle of $\approx 90^\circ$. Although the plume morphology may be more complicated, this is a meaningful framework for studying the relations between scattering properties and brightness. Locally, we modeled the cone surface as a homogeneous plane-parallel layer of scattering fragments that follow a power-law size distribution consistent with grains in samples returned from asteroid Itokawa (Nakamura et al. 2012). We expect the grain sizes present in the plume to range from tens of microns to perhaps several centimeters or larger, although the particle size distribution could differ from the original regolith and depend on impact processing (Cheng et al. 2016). A power-law index $p \approx 3.0$ (i.e., $n(>a) \propto a^{-p}$) is used to define the cumulative grain concentration. Defining a_{\min} and a_{\max} as the limiting radii then results in a normalized differential distribution,

$$\frac{dn}{da} = 3a^{-4} \left[\left(\frac{1}{a_{\min}} \right)^3 - \left(\frac{1}{a_{\max}} \right)^3 \right]^{-1}, \quad (2)$$

where $\int_{a_{\min}}^{a_{\max}} \frac{dn}{da} da = 1$. Plume brightness is sensitive to a_{\min} , since most of the scattered light is emitted by the fine-grain fraction in the size distribution, with brightness increasing as the assumed a_{\min} decreases.

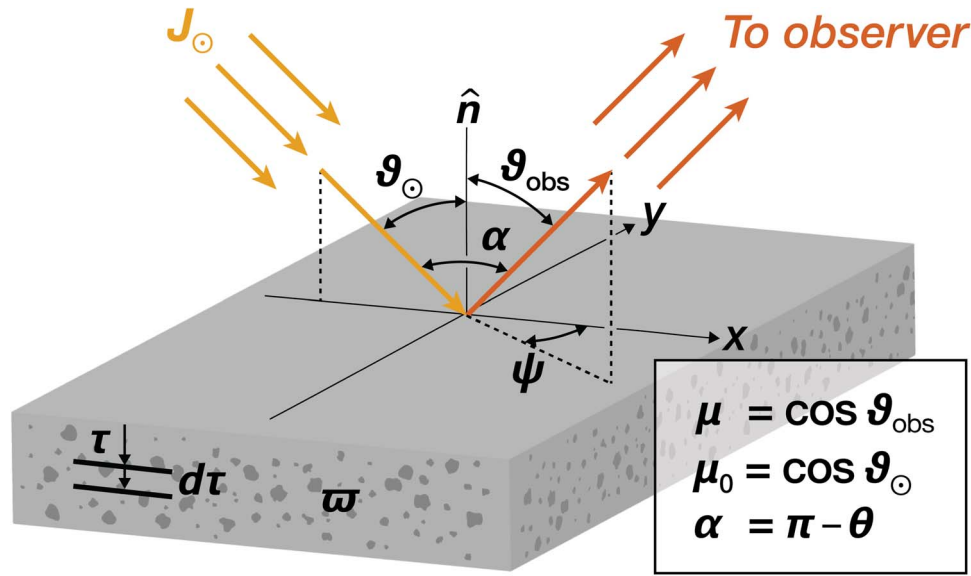


Figure 2. Scattering geometry for the plume, where J_{\odot} is the solar irradiance, \hat{n} is the plume surface normal, ϑ_{\odot} is the solar zenith angle, ϑ_{obs} is the observer emission zenith angle, ψ is the observer azimuth angle, and α is the phase angle. The path enhancement factor through the layer is defined as μ and μ_0 for the emission and solar zenith angles, respectively. Optical depth is given by τ , with particle single-scattering albedo indicated by ϖ .

Quantitative estimates for plume scattering intensity require a model for the angular scattering phase function $F_{11}(\theta)$, which defines the first term in the Mueller matrix (a size-independent model is adopted), as well as estimates for grain scattering and extinction efficiencies, defined by Q_{sca} and Q_{ext} , respectively. For an ensemble of randomly oriented grains, the phase function is azimuthally symmetric and depends only on scattering angle θ or, equivalently, the phase angle $\alpha = \pi - \theta$, and is normalized to 4π over a sphere. Since the integration over azimuth equals 2π , this reduces to

$$\int_0^\pi F_{11}(\theta) \sin(\theta) d\theta = 2. \quad (3)$$

The ratio $F_{11}(\theta)/4\pi$ can then be interpreted as the probability (sr^{-1}) of scattering into direction θ . The layer is characterized by a single-scattering albedo ϖ following the usual definition, i.e., $\varpi = Q_{\text{sca}}/Q_{\text{ext}}$.

The scattering geometry is shown in Figure 2, with J_{\odot} the solar irradiance, \hat{n} the plume surface normal, and ϑ_{\odot} and ϑ_{obs} the solar zenith angle and observer emission angle. Scattering angle (θ) is omitted for clarity in the diagram. Azimuth angle ψ is relevant for multiple-scattering computations, as discussed below. Optical depth τ is increasing in the downward direction. The contributions to scattering in the layer interior consist of volume emission and absorption of scattered photons plus a single-scattering term from the attenuated source beam (see, for example, Hapke 2012). In the optically thin limit, only the single-scattering term is nonnegligible, and the radiative transfer equation reduces to

$$-\mu \frac{dI(\tau, \alpha)}{d\tau} = J_{\odot} \varpi \frac{F_{11}(\alpha)}{4\pi} e^{-\tau/\mu_0}. \quad (4)$$

Note that $d\tau/\mu$ is always negative, and the last factor is ≈ 1.0 . Integration of Equation (4) leads to

$$I(\alpha) = J_{\odot} \frac{\tau}{\mu} \varpi \frac{F_{11}(\alpha)}{4\pi}. \quad (5)$$

Since plume particles are much larger than the observing wavelength, scattering properties can be described using

geometric (or “ray trace”) optics with added diffraction (Macke 2000; Muinonen et al. 2009). The grain scattering coefficient is the sum of geometric $Q_{\text{sca}}^{\text{G}}$ and diffraction $Q_{\text{sca}}^{\text{d}}$ contributions, where $Q_{\text{sca}}^{\text{d}} = 1$ for large, isolated grains. The extinction (geometric scattering + absorption + diffraction) coefficient $Q_{\text{ext}} = 2$ (the “Extinction Paradox” described by van de Hulst 1981). Corresponding scattering cross sections C_{sca} and C_{ext} are $\sigma_a(Q_{\text{sca}}^{\text{G}} + Q_{\text{sca}}^{\text{d}})$ and $\sigma_a Q_{\text{ext}}$, with σ_a the spherical-equivalent cross section of the particle. The grain single-scattering albedo, following from the definition above, becomes $\varpi = C_{\text{sca}}/C_{\text{ext}} = Q_{\text{sca}}/Q_{\text{ext}}$. The phase function is the weighted sum of the geometric and diffraction contributions, with the latter computed by summing diffraction envelopes (Allen 1946; Hapke 2012) over the assumed size distribution, weighted according to grain physical area,

$$F_{11}(\alpha) = \frac{Q_{\text{sca}}^{\text{G}}}{Q_{\text{sca}}} F_{11}(\alpha)^{\text{G}} + \frac{Q_{\text{sca}}^{\text{d}}}{Q_{\text{sca}}} \left\langle F_{11}^{\text{d}}(a, \alpha) a^2 \frac{dn}{da} \right\rangle. \quad (6)$$

For a scattering layer with total grain concentration N per unit area, the extinction optical depth is Q_{ext} multiplied by the physical optical depth, or

$$\tau = N Q_{\text{ext}} \int_{a_{\text{min}}}^{a_{\text{max}}} \sigma_a \left(\frac{dn}{da} \right). \quad (7)$$

An observable measure of brightness is geometric albedo (A_p), defined as the ratio of the zero phase brightness of an object to that of an ideal Lambert disk (Hanner et al. 1981; Hapke 2012). Noting that the zero phase brightness of a grain is $J_{\odot} \sigma_a \varpi (F_{11}(0)/4\pi)$ and that of a Lambert disk is $A_p \sigma_a (J_{\odot}/\pi)$ leads to a relation between the two definitions of albedo, $\varpi = 2A_p/F_{11}(0)$. Given the range of grain size expected in the DART impact plume ($a > \text{tens of microns}$), the diffraction contribution will be confined to scattering angles within a few degrees of zero and hence unobservable by LICIAcube. Diffraction can therefore be legitimately ignored in brightness estimates, which results in a simplified but equally valid rescaling of the scattering parameters, with $Q_{\text{sca}}^{\text{d}} = 0$ and

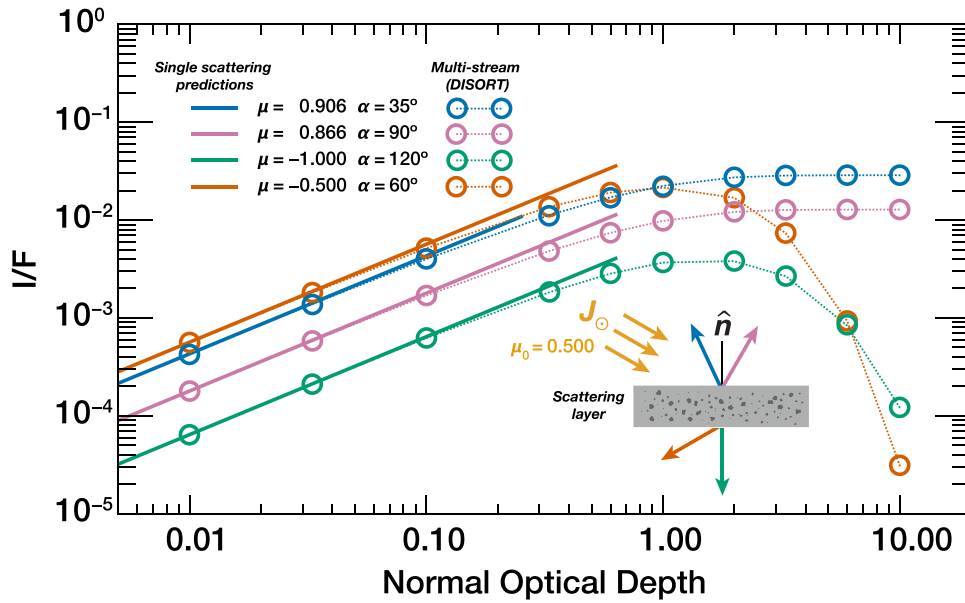


Figure 3. Comparison of single- and multiple-scattering results for reflection and transmission cases that would be typical of the LICIAcube flyby. The scattering properties in these examples are those of a plume particle analog described in Section 3 (large MgFeAlSi grains). The inset diagram shows Sun and observer directions for model results. Given the increasing divergence between the single- and multiple-scattering results, it is apparent that for most geometries, multiple-scattering computations will be necessary for relating measured line-of-sight (LOS) brightness to plume optical depth and therefore mass.

$Q_{\text{ext}} = 1$. In this case, the phase function $F_{11}(\alpha)$ is just the geometrically measured shape $F_{11}^G(\alpha)$, and $\varpi = Q_{\text{sca}} = Q_{\text{sca}}^G$.

2.2. Multiple Scattering

At larger plume optical depths ($\tau > \sim 0.1$), it is necessary to account for the multiple-scattering terms in the radiative transfer equation. We accomplished this using a discrete ordinate multistream code, DISORT (Stamnes et al. 1988), with the phase function represented by a Legendre polynomial expansion. Additional DISORT inputs necessary for computing the scattering intensity are layer τ and ϖ , as well as illumination and observer directions defined relative to the plume surface normal (Figure 2). We used an improved version of the DISORT code (Lin et al. 2018) that accurately accounts for the very strong and narrow diffraction peak by representing the Legendre expansion as a truncated series expansion concatenated with a series of suitably weighted higher-order terms. Numerical testing at small optical depths ($\tau < 0.10$), where both methods can be meaningfully compared, shows that results using 48 streams and 180 Legendre moments accurately reproduce the analytically computed brightness (Equation (5)).

This is verified in Figure 3, which compares single-scattering approximations with multiple-scattering predictions for observing geometries typical of those expected during the LICIAcube flyby. The solar zenith angle is fixed at 60° in these examples, which include both reflection and transmission cases. Phase function shape and single-scattering albedo belong to one of the scattering analogs described in Section 3 (MgFeAlSi grains, $\varpi = 0.575$). These results show the scattering contributions from a plume by itself and do not include multiple-scattering contributions from an underlying surface. Single-scattering estimates can be used to relate brightness to optical depth up to perhaps $\tau \sim 0.10$, but these become nonphysical at larger values, and multiple scattering must be taken into account.

An additional (albeit approximate) check can be made on the validity of the optically thick result by replacing τ in

Equation (5) with the factor $1 - e^{-\tau}$, which becomes 1.0 when τ is large. Noting that $F_{11}(\alpha = 35^\circ) = 0.272$ for MgFeAlSi particles results in $I/F \approx 0.043$, a value $\approx 50\%$ larger than the asymptotic ($\tau = 10$) multiple-scattering result. This difference is largely explained by the fact that the scattering contributions from underlying thin layers that make up the plume will be attenuated by the overlying ones.

We also investigated the effect on the transition from single to multiple scattering of increasing ϖ (single-scattering albedo) for the MgFeAlSi grains (i.e., the optical depth at which the single- and multiple-scattering curves diverge). We did not find a significant change in the fractional departure in optical depth when ϖ was increased to 1.0 (less than a few percent). In general, we do not believe that further numerical tests are needed to answer this question, since the analogs studied here are much darker.

2.3. LICIAcube Observing Geometry

To examine brightness as a function of optical depth during the LICIAcube flyby of Dimorphos, we adopt the DART coordinate system described by Cheng et al. (2020), wherein the trajectories of DART and LICIAcube define the reference x - y plane, and t is the elapsed time from impact (Figure 4). The LOS simulations lie in the x - y plane and intersect the plume surfaces along the $+x$ and $-x$ axes. These coordinates are transformed to plume surface coordinates in order to compute intensities as described above. See Appendix A for additional details.

3. Phase Curve Modeling

In order to examine the variability in the model brightness versus the optical depth relation, we examine several candidate geometric phase functions, along with an unrealistically bright isotropic function as described below.

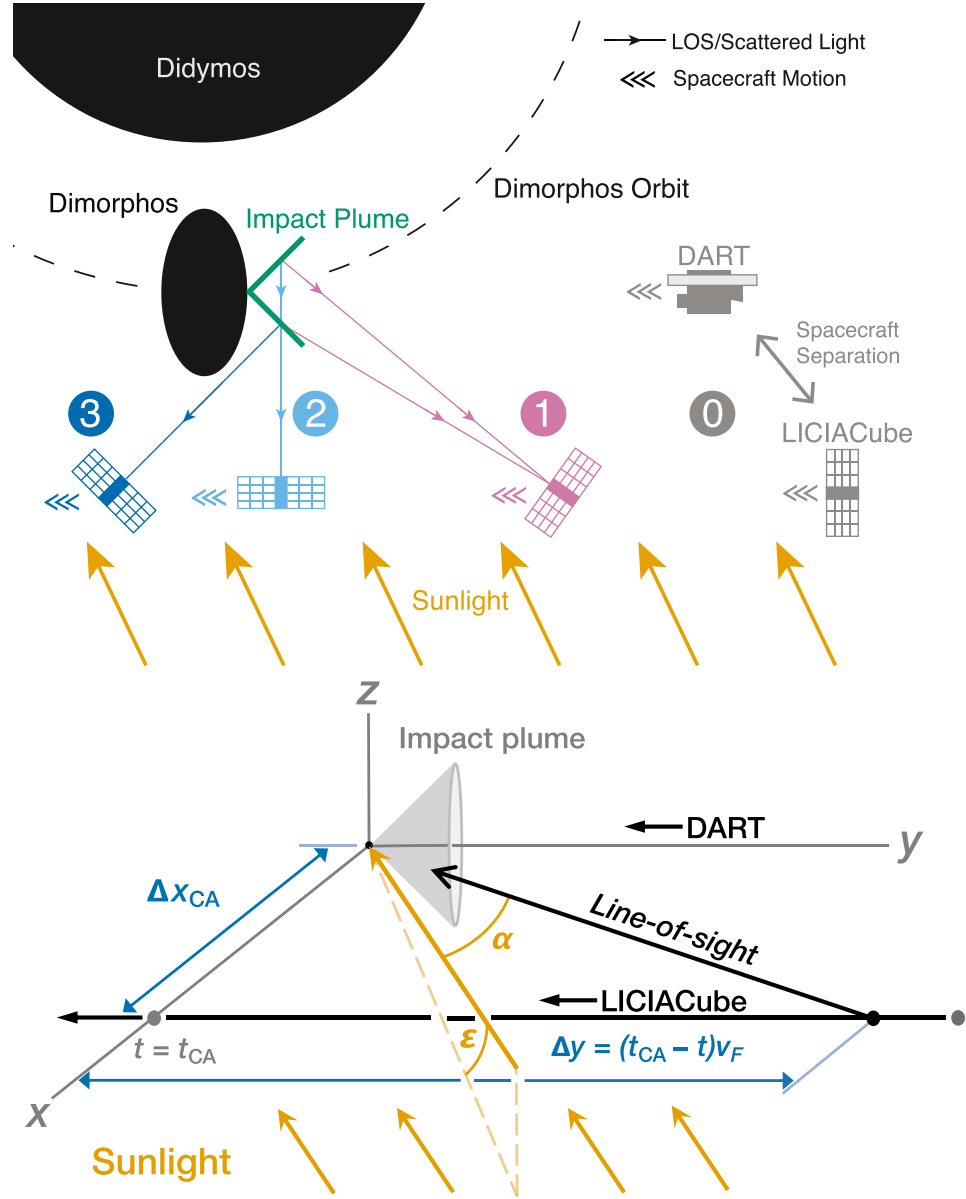


Figure 4. (Top) Simplified version of LICIACube evolving viewing geometry. This shows the LICIACube separation from the DART spacecraft (0) and simulated times/locations along the LICIACube trajectory used in this study (1–3). (Bottom) LICIACube encounter with evolving optical scattering geometry. LICIACube flyby geometry based on Cheng et al. (2020); origin at impact and ejecta plume centered on y-axis. The LOS is the reverse of the position vector (as a function of time) of LICIACube; v_F is the relative velocity of LICIACube; Δx_{CA} is the distance from the origin at closest approach ($t = t_{CA} = 167$ s); α is the phase angle, i.e., $180^\circ - \theta$, where θ is the scattering angle; and ϵ is the Sun elevation angle.

Isotropic—This is the simplest case, as used in Cheng et al. (2020). Here $F_{11}^G = 1$ everywhere, and $Q_{sca}^G = 4A_p$ given that $A_p = 0.15$.

Constant phase coefficient—As proposed by Fahnestock et al. (2022), the model assumes a constant phase coefficient C_p , defined as the negative log slope of brightness,

$$C_p = \frac{dm}{d\alpha} = -2.5 \frac{d}{d\alpha} \log_{10}(F_{11}(\alpha)), \quad (8)$$

where the assumed fixed value of $C_p = 0.013$ (magnitudes per degree) is the average of the “best observed” values for naturally ejected millimeter-sized particles from Bennu (Hergenrother et al. 2020). Then, F_{11} has the form

$$F_{11}(\alpha) = F_{11}(0) 10^{-0.4C_p\alpha}, \quad (9)$$

where α is given in degrees. Solving analytically for $F_{11}(\alpha)$, assuming once again a geometric albedo of 0.15 and applying the normalization of 4π , gives $F_{11}(0) = 2.636$ with a corresponding geometric scattering coefficient, $Q_{sca}^G = 0.228$.

Millimeter-grain models—For the geometric component, we used laboratory-measured phase curves for two large-grain (several millimeters) dust analogs selected from a larger family of samples, shown in Figure 5. Phase curves for the volcanic (Etna) and quartz grains were taken from the measurements of Muñoz et al. (2017) and for the MgFeAlSi (aluminosilicate), charcoal, dusty porous ball (DPB), and quartzite grains from the measurements of Muñoz et al. (2020). We obtained the data for these phase curves from the Amsterdam–Granada database (<https://www.iaa.csic.es/scattering/>; Muñoz et al. 2012). Muñoz et al. (2017, 2020) acquired measurements between

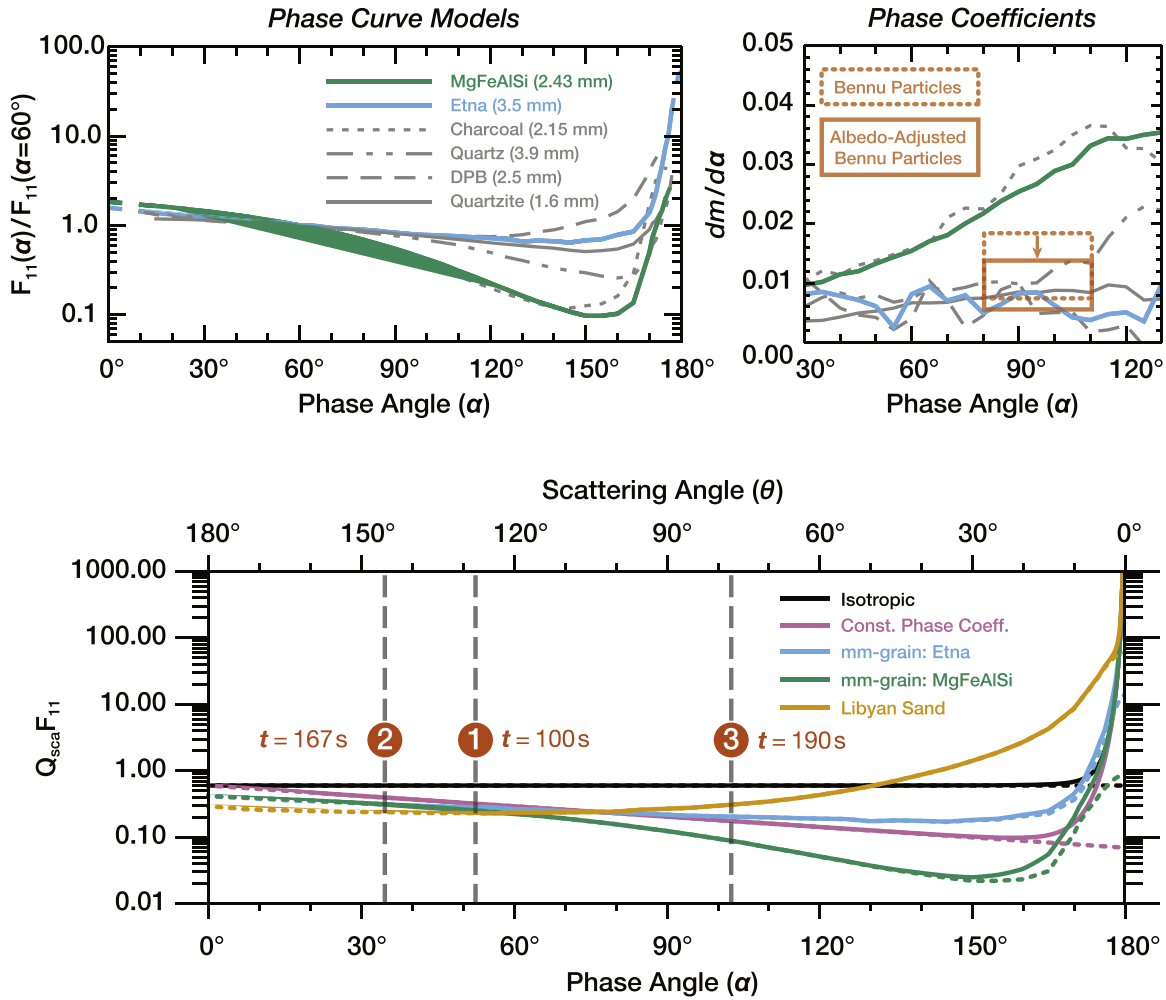


Figure 5. (Top left) Sample phase curves from lab measurements by Muñoz et al. (2017, 2020) of large- (millimeter-) grain porous (Etna) and compact (MgFeAlSi) particles (blue and green, respectively) and part of a set of large-particle samples. These can be considered limiting cases for the scattering behavior of DART impact fragments. (Top right) We calculated phase coefficients for each lab-measured curve. The Etna curve lies at the lower end of the values from Benu particle photometry (Hergenrother et al. 2020) after a correction for the higher albedo of the Didymos/Dimorphos system. Based on this phase coefficient criterion, we selected the Etna particle to represent a dark particle extreme, while the MgFeAlSi curve represents a bright particle extreme. (Bottom) Comparison between phase curve models with diffraction (solid) and without (dotted).

520 and 527 nm, and we deemed these broadly applicable for visible-wavelength scattering, although wavelength dependence is not considered closely in this study. The chosen models (Etna and MgFeAlSi) represent examples of porous and compact particles and can be considered limiting cases for the scattering behavior of DART impact fragments. The dark volcanic Etna sample exhibits moderate porosity and a rough surface. Between $\alpha = 80^\circ$ and 110° , the phase coefficient is small and within the range of values for naturally ejected Benu particles with a best-fit density of $\approx 1340 \text{ kg m}^{-3}$ (Hergenrother et al. 2020) after an $\approx 25\%$ downward correction to account for the higher albedo of Didymos/Dimorphos (Hergenrother et al. 2013). The aluminosilicate (MgFeAlSi) sample is more compact, exhibiting a phase coefficient more closely resembling the disk function of larger objects from $\alpha \approx 90^\circ$ up to the inflection point near $\alpha = 140^\circ$. All samples are otherwise characterized by flat side-scattering and pronounced forward-scattering lobes. Muñoz et al. argued that the observed forward scattering is likely the result of surface roughness at wavelength scales. No evidence for opposition brightening is observed in the Etna particle up to the experimental cutoff angle of about 10° in phase angle. In the case of MgFeAlSi, the

two small phase data points suggest some brightening, but it is not clear whether this is a real trend or measurement scatter. In both cases, we extrapolate to $\alpha = 0^\circ$ by linear fitting to $dm/d\alpha$. The authors acknowledge that some additional opposition brightening (up to $\Delta m \approx 0.4$) may be present, in excess of that predicted by the small but nonzero measured phase coefficients ($dm/d\alpha \approx 0.008\text{--}0.010$). Hergenrother et al. (2020) reached similar conclusions in a photometric analysis of side scattering from Benu ejected particles. We extrapolate to $\alpha = 180^\circ$ (forward scattering) by matching the high phase measurements to a scaled Henyey–Greenstein shape.

Libyan sand grains (fine grains)—To represent a possible fine-grain population among the plume fragments, we include the phase function shape from Libyan sand grains (area-weighted effective radius, $a_{\text{eff}} \approx 125 \mu\text{m}$) as shown in Figure 5 and described by Muñoz et al. (2007), distinct from an “Old Sahara” sample of yet smaller grains (Nousiainen et al. 2011). The size distribution of the Libyan sand grains was measured by those authors and fit to a trimodal, lognormal size distribution. Few, if any, grains exist at radii $< 10 \mu\text{m}$, so they truncated the distribution there. As with the millimeter grains, the shape is interpolated using a fine grid and then extended to

$\alpha = 0^\circ$ using a linear fit to $dm/d\alpha$ and to $\alpha = 180^\circ$ via a matched Henyey–Greenstein shape. The completed shape is then renormalized to 4π , with the result $F_{11}(0) = 0.435$. Since all grains are well in the geometric size regime, we obtain the geometric scattering coefficient as before and find that it is not possible for one of these grains, viewed at $\alpha = 0$, to appear brighter than $A_p \approx 0.11$. Comparisons of this data set with the results of ray optics with diffuse and specular interactions models by Nousiainen et al. (2011; their Table 3) indicate $\varpi \approx 0.69^{+0.22}_{-0.05}$, corresponding to $A_p \approx 0.073^{+0.023}_{-0.005}$. Such models depend on the choice of refractive index for the host grain, as well as the properties and concentration of the wavelength-scale internal and external surface scatterers.

4. Brightness Simulations from the LICIAcube Perspective

As stated in the Introduction (Section 1), the purpose of this study is to create a plausible set of scattering properties, rather than focus on predicting plume radiance or areal mass. For this reason, we limit our results to a simple parameterization of brightness versus optical depth. They confirm that the choice of scattering properties will have a large influence on the relation between measured brightness and inferred plume mass, as demonstrated below. We predicted the LOS plume brightness observed by LICIAcube cameras in the x - y plane as a function of extinction optical depth for a representative set of three time steps during the encounter, one from in front of the plume, one from the side, and one from behind. Figure 6 shows the results, plotted as brightness in magnitudes per square arcsecond. These are presented for the candidate phase curves discussed above (Section 3), the isotropic, constant phase coefficient, limiting millimeter grain curves (MgFeAlSi and Etna), and Libyan sand models.

Step 1 ($t = 100$ s, $\alpha = 52.6^\circ$; Figure 6, top)—LICIAcube observes the plume from the front, as shown in the schematic on the left-hand side. We model beams I_a (red) and I_b (blue) from plume surfaces a (far side) and b (near side). At this time step, brightness predictions for all scattering analogs are consistent within a factor of 2, the exception being the isotropic case (see also Figure 5, bottom). There is some divergence between cases at larger optical depths, particularly for plume b , which is observed in transmission. In the fine-grains case (Libyan sand), higher reflectance at large optical depths is an indirect consequence of stronger forward scattering, since grains at deeper layers reflect the light from those above them.

Step 2 ($t = 167$ s, $\alpha = 34.9^\circ$; Figure 6, middle)—LICIAcube observes the plume from the side and sees the radiance I'_b , which is the superposition of I_b and I_a attenuated by transmission through plume surface b given by $I'_b = I_b + I_a e^{-\tau/\mu_b}$. For this simplified plume geometry, we ignore possible multiple-scattering effects that may occur between plumes a and b . The results are similar to the previous time step, though an increase in divergence between the curves is seen at lower optical depths when compared with the previous result. Again, isotropic scatterers are the significant outlier.

Step 3 ($t = 190$ s, $\alpha = 101.6^\circ$; Figure 6, bottom)—LICIAcube observes the plume from behind. Significant high phase angle divergence between scattering analogs appears. Observed in transmission, a plume consisting of fine grains (Libyan sand) appears notably brighter at all optical depths as a consequence of pronounced forward scattering.

The brightness difference between the isotropic model and more realistic scattering analogs reaches up to an order of magnitude when compared with the dimmest cases: MgFeAlSi for step 1 ($t = 100$ s) and step 3 ($t = 190$ s) and constant phase coefficient for step 2 ($t = 167$ s). This highlights its unsuitability for use with real observations. The large brightness values seen for the Libyan sand case at large optical depths ($\tau_{\text{ext}} > 1.0$) are a consequence of the broad forward-scattering peak, likely the result of efficient surface scattering and increased internally transmitted light in the smaller grains, where the path attenuation is small enough to allow transmission through the grain.

To convert the brightness results to plume areal ejecta mass requires a relation between areal mass M and extinction optical depth τ_{ext} (see derivation in Appendix B). Given a power-law coefficient for cumulative fragment concentration $p = 3.0$, the plume areal mass, M in kg m^{-2} , is

$$M = \frac{4\rho}{3} (\ln a_{\text{max}} - \ln a_{\text{min}}) \frac{a_{\text{min}} a_{\text{max}}}{a_{\text{max}} - a_{\text{min}}} \cdot \frac{\tau_{\text{ext}}}{Q_{\text{ext}}}, \quad (10)$$

where ρ is the fragment mass density in kg m^{-3} , a_{min} and a_{max} define the end points of the size distribution in millimeters, and τ_{ext} is the extinction optical depth.

When combining the M - τ_{ext} relation, Equation (10), with the brightness results from Figure 6, it can be seen that the spread in τ_{ext} resulting from an uncertain phase function shape creates an accompanying uncertainty in plume mass. Another important parameter choice is the minimum grain size of the size distribution, a_{min} . For any assumed size distribution, the results of such simulations are sensitive to the abundance of the fine-grain population controlled by a_{min} , which can be seen from Equation (10).

The influence of uncertain a_{min} on plume brightness can be estimated using a straightforward simulation. Given a value of plume areal mass M , optical depth τ_{ext} and therefore plume scattered light intensity depends on the choice of a_{min} (as well as the power-law coefficient for the size distribution).

The combined influence of a_{min} and choice of scattering analog on plume brightness is summarized in Figure 7, which shows the predicted I/F versus phase angle (α) for a range of plausible a_{min} values (0.03–1.0 mm) and phase functions (compact and porous grains). Areal mass M and grain density ρ are fixed in these plots at 1 kg m^{-2} (a moderate value) and 2000 kg m^{-3} , respectively. Taken by itself, the a_{min} variable contributes a factor of 3–4 uncertainty in intensity. This is apparent at small values of the phase angle, where the choice of millimeter-grain phase function will have almost no influence. At high phase angles, however, the total spread in the I/F prediction has increased to a factor of ≈ 20 after compounding with the phase function shapes that have strongly diverged. Although small grains contribute little to the total ejecta mass, they strongly influence plume brightness. Plume brightness in the finest-grain case is close to asymptotic as a result of large τ , and only modest additional brightening occurs (i.e., the plume becomes optically thick). To the extent that all scattering analogs have similar albedos at small phase angles, it follows that observations at small phase will minimize the overall uncertainty in converting observed brightness to plume mass and therefore momentum transfer.

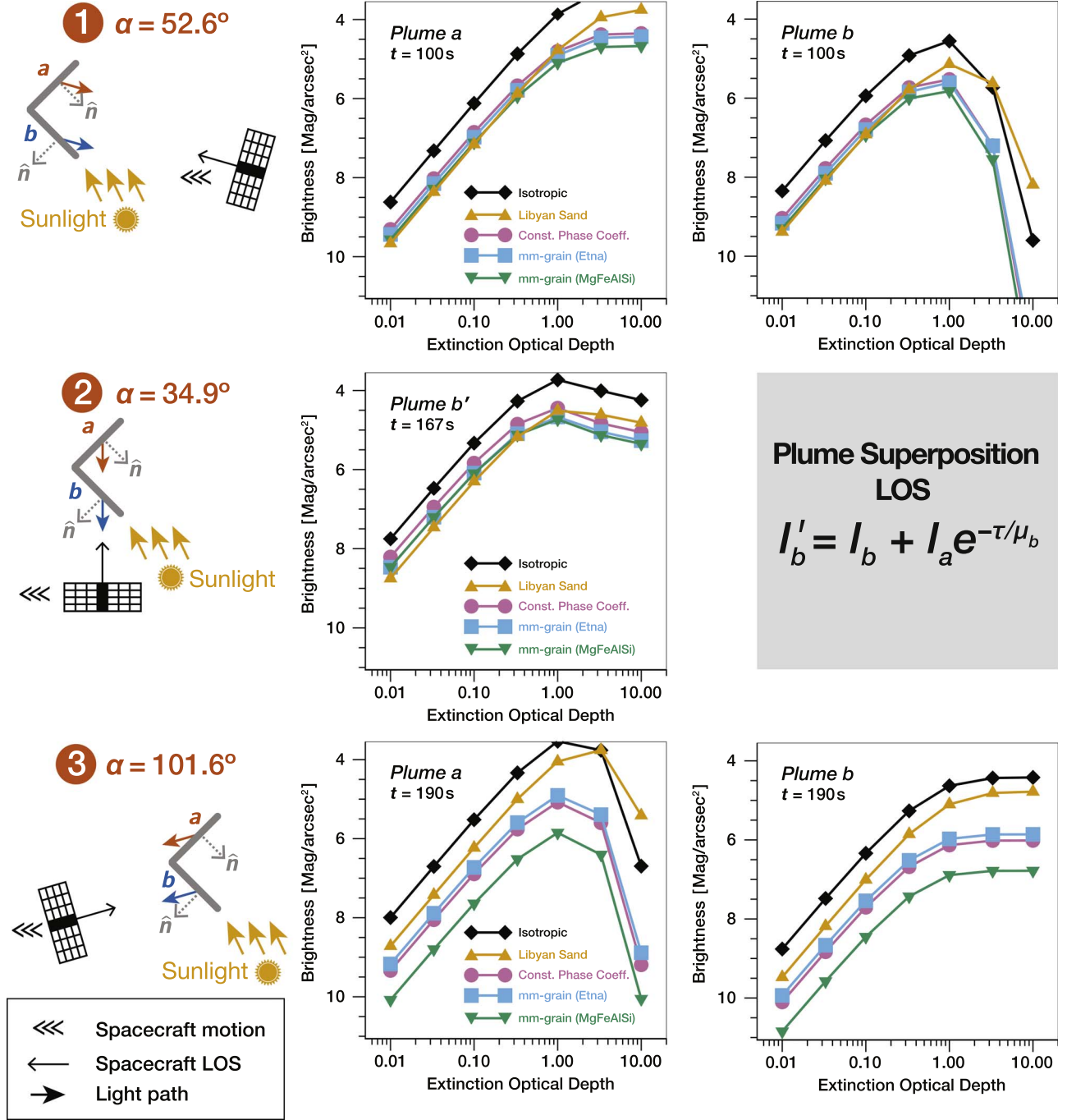


Figure 6. Plume surface brightness as a function of optical depth as viewed by LICIAcube along its flyby trajectory for all five candidate scattering properties models. We modeled two plume surfaces, labeled *a* and *b*. The diagrams depict the observing geometry at each time step, with the corresponding phase angle α given. At $t = 167$ s (CA), the CubeSat views the superposition (I'_b) of *a* and *b*, as illustrated (plume-plume multiple-scattering effects are ignored). The isotropic model appears unrealistically bright under almost all circumstances. For the remaining models, the brightness predictions are similar (within a factor of 2) at small phase angles, though the results diverge dramatically at larger phase angles.

5. Summary

We modeled the visible surface brightness of the DART impact plume as a function of extinction optical depth, τ_{ext} , using the basic conical plume geometry of Cheng et al. (2020) and cumulative size distribution following the steep extension of the Itokawa power-law distribution ($p = 3.0$) as described by Nakamura et al. (2012). We computed brightness simulations from the perspective of LICIAcube at three representative time steps during its flyby: observing from in front of the plume,

from the side, and from behind. As previously stated, the focus of this study has been to estimate plume brightness from the LICIAcube perspective using realistic scattering properties, not to model DART plume evolution, which is the intent of ongoing studies by Cheng et al. (2022), Fahnestock et al. (2022), Kolokolova et al. (2022), and others.

We computed plume brightness using a discrete ordinate, multiple-scattering code (DISORT) that evolved for use with plane-parallel scattering geometries and was found to be entirely suitable and convenient for the constrained geometry in

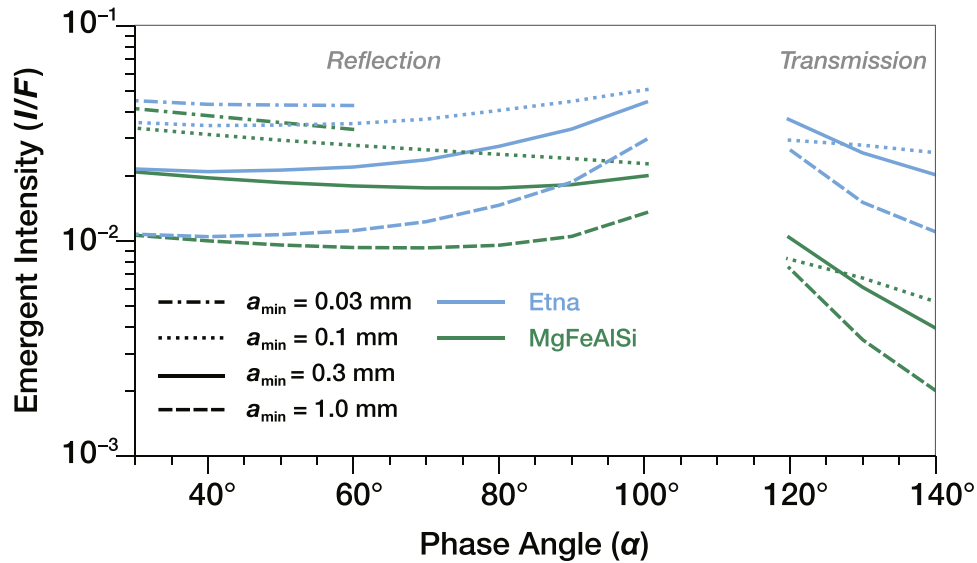


Figure 7. Variability in predicted I/F resulting from the combined uncertainty in a_{\min} (minimum grain size of size distribution) and choice of scattering phase function (millimeter-grain models are used as extreme cases). As a_{\min} decreases, the resulting brightness tends to increase. The solar zenith angle is 20° , and the areal mass of the scattering layer is 1.0 kg m^{-2} . Layer optical depths (τ) range from 0.29 ($a_{\min} = 1.0 \text{ mm}$) to 4.29 ($a_{\min} = 0.03 \text{ mm}$). For clarity, only the first few points are displayed in the $a_{\min} = 0.03 \text{ mm}$ case. In this example, plume brightness in the finest-grain case is close to asymptotic as a result of large τ , and only modest additional brightening occurs.

this study. A comparison of the DISORT results and analytical single-scattering approximations at small optical depths ($\tau < 0.1$), where both methods are valid, showed good agreement between the two methods. More flexible, albeit more complicated, 3D Monte Carlo radiative transfer codes (e.g., HYPERION; Robitaille 2011) will be necessary for modeling the scattering from arbitrary dust geometries and interpreting the LICIACube image data.

We have intercompared brightness predictions from five plausible scattering analogs.

1. *Isotropic.* Used by Cheng et al. (2020, 2022) with a physical albedo assumed for the parent object of $A_p = 0.15$. This significantly overpredicts brightness and therefore underpredicts the LOS dust abundance (and mass) for nearly all observing geometries.
2. *Constant phase coefficient.* As used in Fahnstoeck et al. (2022), this assumes a constant phase coefficient, C_p , and likewise assumes $A_p = 0.15$. This is a significant improvement in approximation over the isotropic case (except at high phase angles) and falls within the envelope of the more realistic millimeter-grain case below.
3. *Millimeter-grain models.* These two related models are the compact MgFeAlSi (aluminosilicate) and porous Etna (volcanic chip) millimeter-grain fragments, with phase function shapes from lab measurements by Muñoz et al. (2017, 2020). We excluded opposition brightening in the phase function and computation of scattering efficiency but acknowledged it as a possibility.
4. *Libyan sand grains (fine grains).* We used the scattering phase function from coarse-grain Libyan sand (Muñoz et al. 2007; Nousiainen et al. 2011) to represent a plume of predominantly fine particles. Geometric scattering from fine grains exhibits strong and broad forward scattering, distinguishing them from larger particles. Grain albedo follows the predictions of ray-optics models (Muinonen et al. 2009; Nousiainen et al. 2011).

This study results in several significant findings relevant to the interpretation of plume brightness images.

1. Plots of brightness versus optical depth indicate that for optically thin layers (normal τ up to perhaps 0.2 or 0.3), one can express reflected I/F as a simple, linear function of the LOS τ , i.e., $I/F = A\tau$, with A an albedo factor. Such a relation enables quick estimates of dust concentration in plume images. A value $A = 0.1$ applies for the isotropic phase function, the phase function considered in Cheng et al. (2020). The remaining scattering analogs illustrated in this study are somewhat dimmer, with A values between 0.04 and 0.05.
2. With the exception of the isotropic case, the range of brightness ($Q_{\text{sca}}F_{11}$) of all scattering analogs studied here lies within a factor of about 2 at phase angles less than 60° – 70° . This result is partly artificial, since the analogs are constrained to assumed values of geometric (zero phase) albedo between 0.15 and 0.07. Larger values in this range result from the inclusion of opposition brightening, which was not directly measured in the laboratory by Muñoz et al. (2017) due to limitations in the instrument scan range. The contribution of opposition brightening is estimated to be ≈ 0.4 mag or less.
3. Predictions of plume optical depth (and therefore brightness) depend on the assumed minimum size (a_{\min}) in the size distribution of impact fragments. At small phase angles, where the influence of phase function is minimal, optical depth increases by about a factor of 4 (at constant plume mass) as a_{\min} is decreased from 1 to 0.03 mm. At large phase angles, brightness estimates are also strongly influenced by divergent phase function shapes. Compounded with the a_{\min} dependence, this leads to uncertainties of up to a factor of ≈ 20 in predicted brightness. Plume observations at small phase angles therefore offer the best prospects for minimizing

uncertainty in the translation from measured LOS brightness to plume mass.

This research was supported by the NASA/GSFC Internal Scientist Funding Model (ISFM) Exospheres, Ionospheres, Magnetospheres Modeling (EIMM) team and the NASA Solar System Exploration Research Virtual Institute (SSERVI). The work done through the Center for Research and Exploration in Space Science and Technology (CRESST-II) is supported by NASA award No. 80GSFC21M0002. L.K. acknowledges support from NASA DART PSP grant 80NSSC21K1131.

Appendix A Adopted Coordinate Frames and LICIACube LOS Observing Geometry

We use a coordinate framework oriented around the CubeSat flyby geometry to simplify relating the plume brightness observed by LICIACube to the scattering properties. We adopt the coordinate system defined by Cheng et al. (2020), wherein the trajectories of DART and LICIACube define the x - y plane, and DART travels along the negative y -axis, bisecting an idealized conical impact plume with an opening angle of 90° . The LICIACube–Dimorphos close-approach (CA) vector lies along the x -axis. This geometry is illustrated in Figure 4 (bottom) and repeated below in Figure 8 (left) with additional annotation.

Table 2 lists the position and velocity information we obtained (or derived) from 2021 July SPICE models describing the LICIACube trajectory. Time t is the elapsed time from

impact. These values are representative only. By coincidence, the initial direction of the Sun in our model was aligned almost exactly on the plume b surface and hence unphysical for our layer geometry. Therefore, we adjusted the Sun vector downward to lie closer to the x - y plane.

Expressed in the reference frame, the Dimorphos-to-LICIACube vector $\mathbf{v}_L(t)$ is

$$\mathbf{v}_L(t) = \begin{pmatrix} \Delta x_{CA} \\ (t_{CA} - t)|\mathbf{v}_F| \\ 0 \end{pmatrix}, \quad (\text{A1})$$

and the corresponding unit pointer $\mathbf{v}_L(t)/|\mathbf{v}_L(t)|$ is designated $\hat{\mathbf{p}}_L(t)$. To follow the convention used by the DISORT radiative transfer code (and get the correct local azimuth), the Sun direction $\hat{\mathbf{p}}_\odot$ has been defined as inward-pointing. Thus, in the reference frame, $\hat{\mathbf{p}}_\odot$ is

$$\hat{\mathbf{p}}_\odot = - \begin{pmatrix} \cos \varepsilon \cos \phi \\ \cos \varepsilon \sin \phi \\ \sin \varepsilon \end{pmatrix}, \quad (\text{A2})$$

where the azimuth angle ϕ is obtained from \mathbb{PA} and ε using spherical triangles, i.e., $\sin \phi = \cos \mathbb{PA} / \cos \varepsilon$. The observer (LICIACube) phase angle α_t is then determined by the dot product of these unit vectors, $\cos \alpha_t = -\hat{\mathbf{p}}_L(t) \cdot \hat{\mathbf{p}}_\odot$.

The DISORT radiative transfer code used in the brightness simulations is suitable only for plane-parallel scattering geometries. Therefore, we carry out calculations of plume

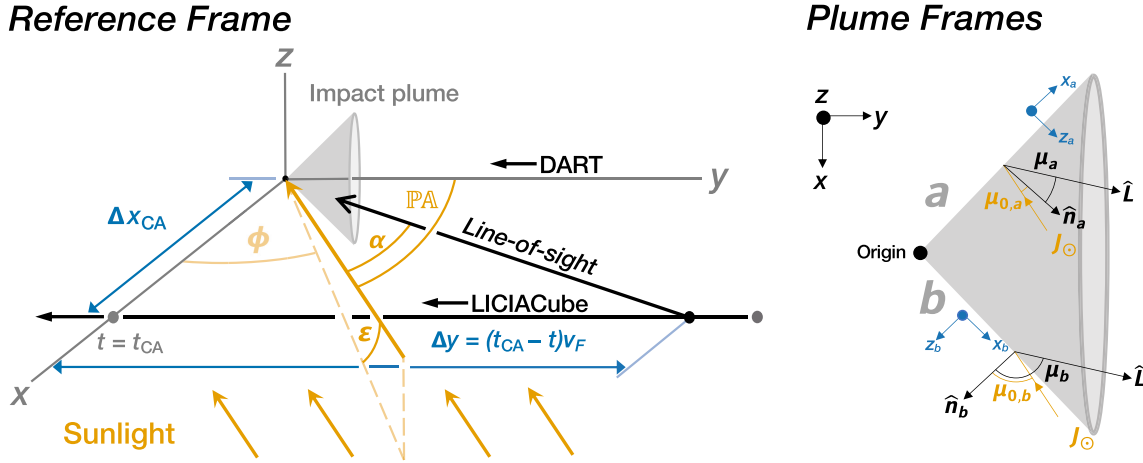


Figure 8. Flyby geometry adopted for the scattering simulations.

Table 2
Flyby Geometry Parameters

Parameter	Symbol	Value	Unit
LICIACube CA distance	Δx_{CA}	51.1	km
CA elapsed time from impact	t_{CA}	167	s
LICIACube, y-axis velocity component	\mathbf{v}_F	-6.15	km s ⁻¹
DART approach phase angle	\mathbb{PA}	59.3	deg
Sun out-of-plane angle	ε	15.0	deg
Sun azimuth angle	ϕ	33.6	deg
LICIACube imaging phase angle	α_t	...	deg

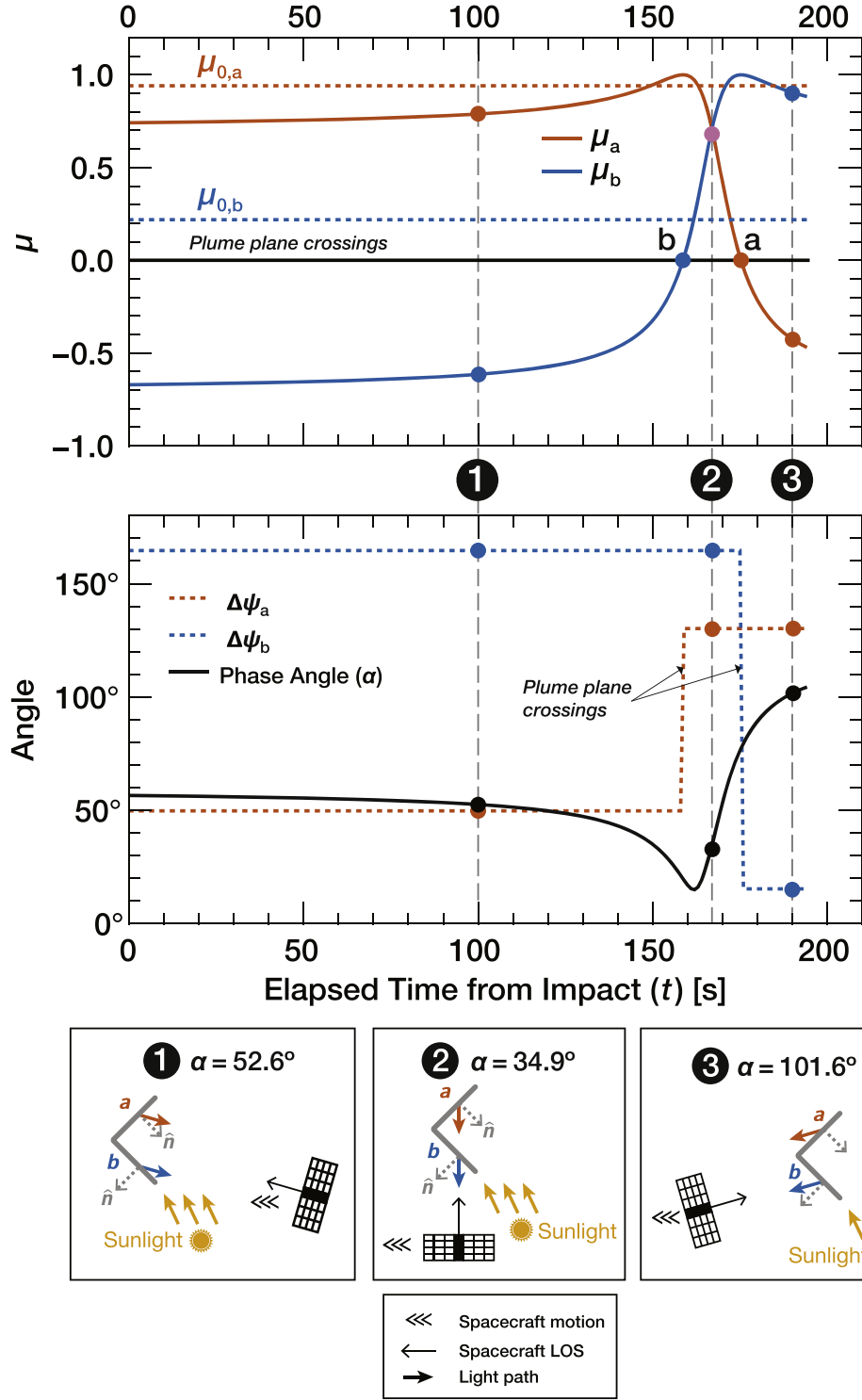


Figure 9. Time evolution of the scattering geometry. For numerical values, see Table 3.

brightness in rotated frames local to plume surfaces a and b (Figure 8, right). The simulations have been further confined to the x - y plane, so that any vector defined in the reference frame is represented in the plume frames via simple rotations,

$$\mathbf{R}_a = \begin{pmatrix} -\cos \pi/4 & \cos \pi/4 & 0 \\ 0 & 0 & 1 \\ \cos \pi/4 & \cos \pi/4 & 0 \end{pmatrix} \quad (\text{A3})$$

and

$$\mathbf{R}_b = \begin{pmatrix} \cos \pi/4 & \cos \pi/4 & 0 \\ 0 & 0 & 1 \\ \cos \pi/4 & -\cos \pi/4 & 0 \end{pmatrix}. \quad (\text{A4})$$

In the plume frames, the spacecraft and Sun pointers become $\hat{\mathbf{p}}_{L,a} = \mathbf{R}_a \hat{\mathbf{p}}_L$ and $\hat{\mathbf{p}}_{\odot,a} = \mathbf{R}_a \hat{\mathbf{p}}_{\odot}$, with similar notation for the b surface. The remaining quantities used in scattering

Table 3
DISORT Model Geometry

t (s)	α (deg)	$\mu_{0,a}$	$\psi_{0,a}$ (deg)	μ_a	ψ_a (deg)	$\mu_{0,b}$	$\psi_{0,b}$ (deg)	μ_b	ψ_b (deg)
100	52.6	0.941	0	0.789	49.8	0.219	0	-0.615	164.6
167	34.9	0.941	0	0.707	130.2	0.219	0	0.707	164.6
190	101.6	0.941	0	-0.425	130.2	0.219	0	0.905	15.4

computations follow from the usual reflectance definitions. In the plume frames, the cosines of the observer zenith angles μ_a , μ_b are just the z -components of the observer pointers

$$\begin{aligned}\mu_a &= [\hat{\mathbf{p}}_{L,a}(t)]_z \\ \mu_b &= [\hat{\mathbf{p}}_{L,b}(t)]_z,\end{aligned}\quad (\text{A5})$$

and, accounting for pointing direction, the same applies for the solar zenith angles,

$$\begin{aligned}\mu_{0,a} &= -[\hat{\mathbf{p}}_{\odot,a}]_z \\ \mu_{0,b} &= -[\hat{\mathbf{p}}_{\odot,b}]_z.\end{aligned}\quad (\text{A6})$$

Defining the solar azimuth angle as zero (always legitimate, since the phase function is azimuthally symmetric), the azimuth angle ψ is just the smaller of the difference angles between projections of these vectors on the plume surfaces. Writing vector projections in the form

$$\hat{\mathbf{v}}_{x-y} = ([\hat{\mathbf{p}}]_x, [\hat{\mathbf{p}}]_y, 0) \quad (\text{A7})$$

and

$$\hat{\mathbf{p}}_{x-y} = \frac{\hat{\mathbf{v}}_{x-y}}{|\hat{\mathbf{v}}_{x-y}|}. \quad (\text{A8})$$

We then find the difference azimuth for plume surfaces a or b from

$$\cos \psi = \hat{\mathbf{p}}_{L,x-y} \cdot \hat{\mathbf{p}}_{\odot,x-y}. \quad (\text{A9})$$

Figure 9 shows the time evolution of the pointing information. Three time steps, 100, 167, and 190 s, are used for the scattering computations, representing forward-, side-, and backscattering geometries. The figure includes pointing information for each instance. Table 3 shows the resulting DISORT model geometry we used for each time step.

Appendix B

Plume Areal Mass-to-Optical Depth Relations

The cumulative fragment size distribution, valid from particle radius $a < 0.001$ to ~ 1 m, can be expressed as

$$\int_{a_{\min}}^{a_{\max}} \frac{dn}{da} da \propto a^{-p}, \quad (\text{B1})$$

where $p \approx 3.0$ is the power-law size coefficient adapted from Cheng et al. (2020) based on the measured boulder size distributions on Itokawa and consistent with Hayabusa2 returned small-grain samples (Nakamura et al. 2012).

Using Equation (B1), one obtains the differential size distribution dn/da normalized to unity:

$$\frac{dn}{da} = S a^{-(p+1)} \quad S \int_{a_{\min}}^{a_{\max}} a^{-(p+1)} da = 1. \quad (\text{B2})$$

Solving and eliminating S gives

$$\frac{dn}{da} = \frac{p a^{-(p+1)}}{a_{\min}^{-p} - a_{\max}^{-p}}. \quad (\text{B3})$$

Defining grain mass density ρ (kg m^{-3}), the concentration of plume fragments is also related to plume areal mass. For unit mass concentration $M_0 = 1 \text{ kg m}^{-2}$, this relation is

$$M_0 = 1 = \int_{a_{\min}}^{a_{\max}} C \frac{dn}{da} \left(\frac{4}{3} \pi a^3 \rho \right) da, \quad (\text{B4})$$

with C a constant that is determined by solving the integral and rearranging,

$$\frac{1}{C} = \frac{4}{3} \pi \rho \cdot \frac{p}{a_{\min}^{-p} - a_{\max}^{-p}} \int_{a_{\min}}^{a_{\max}} a^{2-p} da, \quad (\text{B5})$$

where the solution to the integral depends on the value of p ,

$$\int_{a_{\min}}^{a_{\max}} a^{2-p} da = \begin{cases} \ln a_{\max} - \ln a_{\min} & p = 3.0 \\ \frac{a_{\max}^{3-3p} - a_{\min}^{3-3p}}{3(1-p)} & p \neq 3.0 \end{cases} \quad (\text{B6})$$

leading to

$$C = \begin{cases} \frac{a_{\min}^{-p} - a_{\max}^{-p}}{4\pi\rho(\ln a_{\max} - \ln a_{\min})} & p = 3.0 \\ \frac{(3-p)(a_{\min}^{-p} - a_{\max}^{-p})}{4\pi\rho(a_{\max}^{3-3p} - a_{\min}^{3-3p})} & p \neq 3.0. \end{cases} \quad (\text{B7})$$

Defining N as the total number of plume particles ($\# \text{ m}^{-2} \text{ m}^{-1}$), we eliminate C by inserting it into Equation B4 to yield the differential number of particles dn/da ($\# \text{ m}^{-2} \text{ m}^{-1} \text{ size}$) for plume areal mass concentration M (km^{-2}):

$$\frac{dN}{da} = MC \cdot \frac{dn}{da} = \begin{cases} M \cdot \frac{3}{4\pi\rho} \cdot \frac{a^{-(p+1)}}{\ln a_{\max} - \ln a_{\min}} & p = 3.0 \\ M \cdot \frac{3-p}{4\pi\rho} \cdot \frac{a^{-(p+1)}}{a_{\max}^{3-p} - a_{\min}^{3-p}} & p \neq 3.0. \end{cases} \quad (\text{B8})$$

B.1. Plume LOS Mass to Optical Depth

We can define an element of geometric optical depth τ_G as

$$d\tau_G = \frac{dn}{da} \pi a^2 da, \quad (\text{B9})$$

where τ_G is related to extinction optical depth τ by $\tau = Q_{\text{ext}}\tau_G$. Integrating Equation (B9) gives

$$\left. \begin{aligned} \tau_G &= M \cdot \frac{3}{4\pi\rho} \cdot \frac{\pi}{\ln a_{\text{max}} - \ln a_{\text{min}}} \int_{a_{\text{min}}}^{a_{\text{max}}} \frac{1}{a^2} da \\ &= M \cdot \frac{3}{4\rho} \cdot \frac{\frac{1}{a_{\text{min}}} - \frac{1}{a_{\text{max}}}}{\ln a_{\text{max}} - \ln a_{\text{min}}} \end{aligned} \right\} p = 3.0 \quad (\text{B10})$$

and


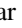
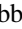

$$\left. \begin{aligned} \tau_G &= M \cdot \frac{3(3-p)}{4\pi\rho} \cdot \frac{\pi}{a_{\text{max}}^{3-p} - a_{\text{min}}^{3-p}} \int_{a_{\text{min}}}^{a_{\text{max}}} \frac{1}{a^2} da \\ &= M \cdot \frac{3}{4\rho} \cdot \frac{\frac{1}{a_{\text{min}}^{3-p}} - \frac{1}{a_{\text{max}}^{3-p}}}{a_{\text{max}}^{3-p} - a_{\text{min}}^{3-p}} \end{aligned} \right\} p \neq 3.0. \quad (\text{B11})$$

Alternatively, we can rearrange these equations to express mass as a function of τ_G :

$$M = \frac{4\rho}{3} (\ln a_{\text{max}} - \ln a_{\text{min}}) \cdot \frac{a_{\text{min}} a_{\text{max}}}{a_{\text{max}} - a_{\text{min}}} \cdot \tau_G \quad p = 3.0, \quad (\text{B12})$$

$$\begin{aligned} M &= \frac{4\rho}{3(3-p)} \\ &\times (a_{\text{max}}^{3-p} - a_{\text{min}}^{3-p}) \cdot \frac{a_{\text{min}} a_{\text{max}}}{a_{\text{max}} - a_{\text{min}}} \cdot \tau_G \quad p \neq 3.0. \end{aligned} \quad (\text{B13})$$

ORCID iDs

Ramin Lolachi  <https://orcid.org/0000-0001-5764-7639>
David A. Glenar  <https://orcid.org/0000-0003-2155-3854>
Timothy J. Stubbs  <https://orcid.org/0000-0002-5524-645X>
Ludmilla Kolokolova  <https://orcid.org/0000-0002-9321-3202>

References

A'Hearn, M. F., Belton, M. J. S., Delamere, W. A., et al. 2005, *Sci*, **310**, 258
Allen, C. W. 1946, *MNRAS*, **106**, 137
Arakawa, M., Saiki, T., Wada, K., et al. 2020, *Sci*, **368**, 67

Cheng, A. F., Michel, P., Jutzi, M., et al. 2016, *P&SS*, **121**, 27
Cheng, A. F., Raducan, S. D., Fahnestock, E. G., et al. 2022, *PSJ*, **3**, 131
Cheng, A. F., Rivkin, A. S., Michel, P., et al. 2018, *P&SS*, **157**, 104
Cheng, A. F., Stickle, A. M., Fahnestock, E. G., et al. 2020, *Icar*, **352**, 113989
de León, J., Licandro, J., Duffard, R., & Serra-Ricart, M. 2006, *AdSpR*, **37**, 178
Dotto, E., Della Corte, V., Amoroso, M., et al. 2021, *P&SS*, **199**, 105185
Escobar-Cerezo, J., Palmer, C., Muñoz, O., et al. 2017, *ApJ*, **838**, 74
Fahnestock, E. G., Cheng, A. F., Ivanovski, S., et al. 2022, *PSJ*, **3**, 206
Farinella, P., & Davis, D. R. 1992, *Icar*, **97**, 111
Feldhacker, J. D., Syal, M. B., Jones, B. A., et al. 2017, *JGCD*, **40**, 2417
Gundlach, B., & Blum, J. 2013, *Icar*, **223**, 479
Hainaut, O. R., Kleyna, J., Sarid, G., et al. 2012, *A&A*, **537**, A69
Hanner, M. S., Giese, R. H., Weiss, K., & Zerull, R. 1981, *A&A*, **104**, 42
Hapke, B. 2012, *Theory of Reflectance and Emittance Spectroscopy* (2nd ed.; Cambridge: Cambridge Univ. Press)
Jewitt, D., Weaver, H., Agarwal, J., Mutchler, M., & Drahus, M. 2010, *Natur*, **467**, 817
Hergenrother, C. W., Maleszewski, C., Li, J. Y., et al. 2020, *JGRE*, **125**, e06381
Hergenrother, C. W., Nolan, M. C., Binzel, R. P., et al. 2013, *Icar*, **226**, 663
Kim, J., Ishiguro, M., Hanayama, H., et al. 2012, *ApJL*, **746**, L11
Kolokolova, L., Li, J. -Y., van Selous, M., Farnham, T. L., & Nagdimunov, L. 2022, *PSJ*, **3**, 262
Lin, Z., Chen, N., Fan, Y., et al. 2018, *JATs*, **75**, 327
Macke, A. 2000, in *Light Scattering by Nonspherical Particles: Theory, Measurements, and Applications*, ed. M. I. Mishchenko, J. W. Hovenier, & L. D. Travis (San Diego, CA: Academic Press), 309
Moreno, F., Licandro, J., Tozzi, G. -P., et al. 2010, *ApJL*, **718**, L132
Muinonen, K., Nousiainen, T., Lindqvist, H., Muñoz, O., & Videen, G. 2009, *JQSRT*, **110**, 1628
Muñoz, O., Moreno, F., Gómez-Martín, J. C., et al. 2020, *ApJS*, **247**, 19
Muñoz, O., Moreno, F., Guirado, D., et al. 2012, *JQSRT*, **113**, 565
Muñoz, O., Moreno, F., Vargas-Martín, F., et al. 2017, *ApJ*, **846**, 85
Muñoz, O., Voltin, H., Hovenier, J. W., et al. 2007, *JGRD*, **112**, D13215
Nagdimunov, L., Kolokolova, L., Wolff, M., A'Hearn, M. F., & Farnham, T. L. 2014, *P&SS*, **100**, 73
Nakamura, E., Makishima, A., Moriguti, T., et al. 2012, *PNAS*, **109**, E624
Nousiainen, T., Muñoz, O., Lindqvist, H., Mauno, P., & Videen, G. 2011, *JQSRT*, **112**, 420
Raducan, S. D., Davison, T. M., & Collins, G. S. 2020, *P&SS*, **180**, 104756
Rainey, E. S. G., Stickle, A. M., Cheng, A. F., et al. 2020, *IJIE*, **142**, 103528
Ritter, B., Karatekin, Ö., Carrasco, J. A., et al. 2021, in 7th IAA Planetary Defense Conf. (Vienna: United Nations Office for Outer Space Affairs), 190
Rivkin, A. S., Chabot, N. L., Stickle, A. M., et al. 2021, *PSJ*, **2**, 173
Robitaille, T. P. 2011, *A&A*, **536**, A79
Snodgrass, C., Tubiana, C., Vincent, J. -B., et al. 2010, *Natur*, **467**, 814
Stamnes, K., Tsay, S. -C., Wiscombe, W., & Jayaweera, K. 1988, *ApOpt*, **27**, 2502
Stickle, A. M., Bruck Syal, M., Cheng, A. F., et al. 2020, *Icar*, **338**, 113446
Stickle, A. M., Rainey, E. S. G., Syal, M. B., et al. 2017, *Procedia Engineering*, **204**, 116
van de Hulst, H. C. 1981, *Light Scattering by Small Particles* (New York: Dover)
Wada, K., Ishibashi, K., Kimura, H., et al. 2021, *A&A*, **647**, A43